

# Description of the Hypo-peritectic Steel Solidification under Continuous Cooling and Crack Susceptibility

José Jorge RUÍZ MONDRAGÓN,<sup>1)</sup> Martín HERRERA TREJO,<sup>1)</sup> Manuel de JESÚS CASTRO ROMÁN<sup>1)</sup> and Hugo SOLÍS T.<sup>2)</sup>

1) CINVESTAV IPN Unidad Saltillo, Carr. Saltillo-Mty Km. 13 Ramos Arizpe, Coah. México. E-mail: jorge.ruiz@cinvestav.edu.mx, martin.herrera@cinvestav.edu.mx, manuel.castro@cinvestav.edu.mx 2) SIDOR, Zona Industrial Matanzas, Edo. Bolívar, Venezuela. E-mail: sirhsy@sidor.com

(Received on November 30, 2007; accepted on January 31, 2008)

This study describes the phase evolution during solidification under continuous cooling conditions of a hypo-peritectic multicomponent steel. Additionally, the mechanical behavior and dimensional variation of the solid–liquid skin were evaluated by using mathematical expressions reported in the literature as a function of the proportion of phases and solute distribution respectively. The crack susceptibility of the solid–liquid skin depended on the proportion of phases and it occurred in two solid fraction regions, independently of the cooling rate. For the region exhibiting the lowest solid fraction values this susceptibility was associated to  $\gamma$  phase, while at the highest solid fraction values it was related to  $\delta$  phase.

At the end of the peritectic transformation the highest contraction observed can be considered as an additional contribution to the crack susceptibility in the solid fraction range of 0.92–0.98. The significant microsegregation of Mn observed for high cooling rates promotes a change in the solidification mode, from a hypo-peritectic mode into a hyper-peritectic mode and the expansion of solid formed from the remaining liquid.

KEY WORDS: solidification; peritectic transformation; carbon steels; mechanical properties; segregation.

## 1. Introduction

It is known that carbon steels with hypo-peritectic composition (carbon content between 0.1 and 0.16 wt%), show surface crack susceptibility when they are produced by the continuous casting process, particularly at high casting rates.<sup>1,2)</sup> Frequently, this susceptibility is attributed to a volumetric contraction associated to the “peritectic solidification”, described by the reaction: liquid (L)+primary phase ( $\delta$ )<sup>3)</sup>→secondary phase ( $\gamma$ ).<sup>2–6)</sup>

It is accepted that the formation of cracks begins during the solidification process in the mold of the continuous casting.<sup>1,4,7)</sup> Therefore, the control of the crack nucleation requires the description of the mechanical behavior of the solidified shell and its dependence on the formed phases. Although some studies have been devoted to the study of mechanical properties at high temperatures, only some of them show a relationship of the mechanical behavior with the evolution of phases during solidification.<sup>8–10)</sup>

The experimental description of phase evolution during solidification in continuous casting is difficult because of the high cooling rates involved. Frequently, mathematical modeling is employed, and several models with different degrees of complexity can be used to describe the solid state diffusion as well as the segregation of solute elements in the liquid.<sup>11,12)</sup> Most of the calculations assume linear cooling rates.

A description of the peritectic solidification for multi-

component steel produced by continuous casting has to consider the solute redistribution because of the relatively high cooling rates employed (2 to 15°C s<sup>-1</sup>). Additionally, the enrichment of the remaining liquid with solute elements can influence significantly its thermal expansion coefficient as well as the local equilibrium conditions at the liquid–solid interface.<sup>5,14,15)</sup>

In order to describe the evolution of phases under continuous cooling conditions, experimental work and mathematical simulation on the solidification of hypo-peritectic multicomponent steel were combined in the present research. Moreover, the mechanical behavior of the solidified shell was described by using mathematical expressions reported in the literature, as a function of the proportion of the formed phases.

## 2. Background

### 2.1. Peritectic Solidification Mechanism

For carbon steels with carbon content between 0.1 and 0.53 wt% when the melt cools down below the liquidus temperature solid nucleates and grows as  $\delta$  phase until  $\gamma$  phase starts to form, *i.e.* peritectic solidification occurs. Currently, it is accepted that the peritectic solidification occurs through two mechanisms, “peritectic reaction” and “peritectic transformation”, shown in **Fig. 1**.<sup>6)</sup> The peritectic solidification starts with the peritectic reaction, in which  $\delta$ ,  $\gamma$  and L phases co-exist and  $\gamma$  phase is formed along the

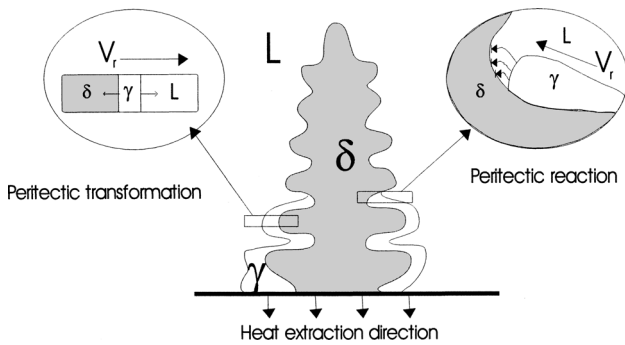


Fig. 1. Mechanism of peritectic solidification.<sup>6)</sup>

$\delta/L$  interface; the solute rejected by the  $\gamma$  phase diffuses through the liquid toward the  $\delta$  phase, contributing to its dissolution. Once the entire  $\delta/L$  interface is covered with  $\gamma$  phase, this forms a barrier separating the primary  $\delta$  phase from the liquid. The growth of  $\gamma$  phase continues throughout the peritectic transformation, at the expense of the  $\delta$  phase, as a result of the occurrence of solid state diffusion. On the other hand, it is possible that under certain conditions the  $\gamma$  phase grows by direct solidification from the liquid.

**2.2. Simulation of the Solidification Process**

The DICTRA program (Diffusion Controlled Transformations)<sup>16)</sup> allows to perform the simulation of diffusive transformations with a moving boundary. It integrates thermodynamics and kinetics databases to solve unidimensional diffusion equations in multicomponent systems, using the Thermocalc<sup>17)</sup> program to calculate the local equilibrium at the involved interfaces.

The volume of control considered for solidification simulation is schematically shown in Fig. 2. A dendritic columnar structure was assumed and the secondary arm spacing,  $\lambda$ , was selected as the characteristic longitude at the microsegregation scale as originally proposed by Brody and Flemings.<sup>11)</sup>

Assuming a regular spacing for the secondary dendrite arms as well as symmetrical properties between them, the volume of control is half  $\lambda$ . The volume of control shows three stages: (1) before the beginning of solidification,  $t=0$ , (2) during primary solidification,  $t=t_1$ , i.e. nucleation and growth of  $\delta$  phase, and (3) during peritectic transformation,  $t=t_2$ .

In order to simulate the growth of the phases during solidification for a given steel, it is necessary to specify the thermal evolution and the secondary dendrite arm spacing,  $\lambda$ . The thermal evolution can be stated by specifying heat flux or cooling rate. In the latter case, a linear cooling rate is frequently assumed; however, an experimental cooling curve can be introduced. The value of  $\lambda$  depends on the cooling rate and it is frequently expressed as a function of the solidification time.

**2.3. Tensile Properties**

The crack susceptibility is a function of the mechanical behavior of solidified shell steel. Mizukami *et al.*<sup>9)</sup> have shown that the tensile strength and elongation during solidification depend on the solid fraction and on the proportion of phases and they have proposed the following equations

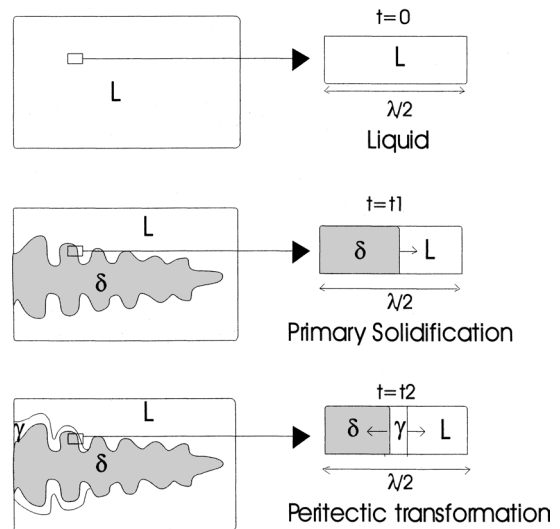


Fig. 2. Volume of control.

for the estimation of these properties:

$$\sigma_{\delta}^{L/S} = 6.0 \times (f_s - 0.8) \times f_{\delta} \dots\dots\dots(1)$$

$$\sigma_{\gamma}^{L/S} = 33.5 \times (f_s - 0.8) \times f_{\gamma} \dots\dots\dots(2)$$

$$\epsilon_{\delta}^{L/S} = 6.5 \times (f_s - 0.8) \times f_{\delta} \dots\dots\dots(3)$$

$$\epsilon_{\gamma}^{L/S} = 6.5 \times (f_s - 0.8) \times f_{\gamma} \dots\dots\dots(4)$$

where  $f_i$  is the fraction of phase  $i$ ;  $i$  can be s,  $\delta$  or  $\gamma$ ;  $\sigma_i^{L/S}$  is the tensile strength and  $\epsilon_i^{L/S}$  is the elongation of phase  $i$ . These equations have been validated for carbon and alloyed steels and solid fractions in the range of 0.8–1.0.<sup>10)</sup>

**2.4. Contraction**

The thermal contraction associated to the phase growth during solidification can be calculated with the aid of a mathematical expression given by Jablonka *et al.*<sup>18)</sup>:

$$\epsilon^{th}(T) = \sqrt[3]{\frac{\rho_{(T_{ref})}}{\rho_{(T)}}} - 1 \dots\dots\dots(5)$$

where  $\epsilon^{th}(T)$  is the thermal contraction at temperature  $T$ ;  $\rho_{(T_{ref})}$  and  $\rho_{(T)}$  are the densities at the reference temperature  $T_{ref}$  and at temperature  $T$ , respectively. In the case of peritectic transformation where several phases are involved, the average density at temperature  $T$  can be calculated with the following expression:

$$\rho_{(T)} = \frac{1}{\sum_{n=1}^p \left( \frac{f_{n(T)}}{\rho_{n(T)}} \right)} \dots\dots\dots(6)$$

where  $f_{n(T)}$  and  $\rho_{n(T)}$  are the phase fraction and density respectively for each one of the  $n$  phases coexisting at temperature  $T$ . The density of the phases can be obtained using the equations suggested by Miettinen,<sup>15)</sup> as a function of temperature and chemical composition.

### 3. Experimental Procedure

In this work the solidification of a multicomponent hypoperitectic steel was studied aiming to describe the growth of phases. In a first stage, a thermal analysis technique was applied for solidification experiments under different continuous cooling conditions in order to obtain the cooling curves as well as characteristic temperatures such as solidification start and starting and ending points of peritectic transformation; the solidification time was also calculated. In the second stage, the software was used to simulate the phase evolution during solidification.

**Figure 3** shows a schematic diagram of the experimental apparatus used to carry out the thermal analyses. The heating device consisted of a vertical resistance furnace fitted with an alumina tube, inside which a movable mechanism supports a crucible containing the melt sample. The movable system was operated by a pneumatic mechanism, allowing the melt sample to slide rapidly along the longitudinal axis. Argon gas was introduced in the upper section of the furnace through an alumina nozzle, just above the crucible. The tip of a B-type thermocouple, protected with a thin ceramic sheath, was introduced into the melt sample up to a depth corresponding approximately to the mid length of the solidified sample. The thermocouple was connected to a data acquisition system in order to record the temperature evolution during the sample cooling. The weight of the sample was approximately 1 g; the solidified sample had a cylindrical shape, with diameter and length of  $0.5 \times 10^{-2}$  and  $1.5 \times 10^{-2}$  m, respectively; these dimensions were selected in such a way as to ensure the heat transport in the radial direction of the melt sample. The crucible charge for the solidification studies consisted in metallic chunks machined from a chemically homogenized sample produced

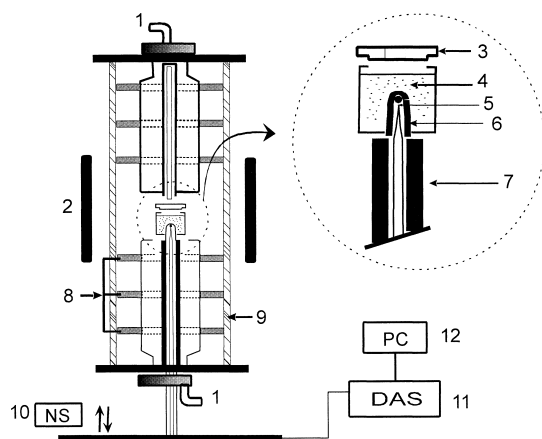


**Fig. 3.** Experimental apparatus, 1) in/out of argon, 2) carbon coil, 3) alumine crucible, 4) melt, 5) B type thermocouple, 6) alumine rod, 7) alumine insulate, 8) thermal screen, 9) alumine tube, 10) neumatic system, 11) data acquisition system and 12) personal computer.

by continuous casting at industrial scale. The chemical composition of this material is given in **Table 1**.

For each solidification test, the samples were sequentially heated, melt and solidified. For the melting stage, the crucible containing the sample was placed in the hottest zone of the alumina tube. After that, the argon gas was introduced and the system was heated at an average rate of  $0.1^\circ\text{C s}^{-1}$  up to  $1530^\circ\text{C}$ , holding it at this temperature for 600 s before solidification started. The solidification conditions were changed for each one of the experiments in order to obtain cooling rates in the range of those found along the width of conventional slabs. The lowest cooling rate was obtained by turning the furnace off and allowing the sample to solidify inside it. High cooling rates were achieved by sliding rapidly the liquid samples to predetermined positions along the alumina tube. The highest cooling rate was achieved by taking the sample out of the alumina tube and allowing it to solidify under ambient air. Five different cooling rates obtained in the manner just described were employed. Each one of the experiments was repeated at least twice in order to corroborate their reproducibility.

For the simulation of the evolution of phases, each one of the cooling rate conditions considered was introduced into the software through the associated cooling curve and the value of the secondary dendrite arm spacing,  $\lambda$ . The  $\lambda$  dimension depends on the cooling condition and it was calculated with the aid of Eq. (7) reported for steels solidified at different cooling rates:

$$\lambda = 26.1 \times t^{0.38} \dots\dots\dots(7)$$

where  $t$  is the solidification time (time elapsed in the solid-liquid region) in s and  $\lambda$  is expressed in  $\mu\text{m}$ .<sup>5)</sup> The  $t$  value was obtained through derivative analysis of the experimental cooling curves. The initial chemical composition considered C, Mn, and Si with contents specified in Table 1, and the initial thickness value for  $\delta$  and  $\gamma$  phase was  $\lambda/20$ . The type of grid used was double geometrical, dividing the region into two halves and generating a separate geometrical grid (300) node in each half, thus allowing contact between the two phases, with one of them acting as an interface for the other one, keeping a uniform interspacing of the grid for a close system.<sup>16)</sup> The software were used<sup>17)</sup> employing the kinetic MOB2 and thermodynamic SSOL data bases.

### 4. Discussion and Results

#### 4.1. Thermal Analysis

**Figure 4** shows the cooling curves obtained for each one of the cooling conditions employed. The calculated cooling rates were in the range for conventional slabs, with the smallest and largest values corresponding to the center and to a region near the surface, respectively; this is in accord

**Table 1.** Chemical composition of steel.

%C	%Mn	%P	%S	%Si	%Al	%Cu	%V
0.13	1.15	0.012	0.005	0.15	0.04	0.15	0.06
%Nb	%Cr	%Mo	%Sn	%Ni	Ti (ppm)	B (ppm)	N (ppm)
0.025	0.1	0.04	0.02	0.1	150	10	80

with estimations carried out from cooling curves simulated and reported by Louhenkilpi *et al.*<sup>19)</sup>

For the evaluation of the cooling rate, given by the difference between the liquidus and solidus temperatures,  $T_l$  and  $T_s$  respectively, divided by the time elapsed in the solid–liquid region,  $t$ , the equilibrium diagram for the studied steel was calculated by using the software,<sup>17)</sup> Fig. 5. From this diagram, the starting and ending temperature of solidification and peritectic transformation were obtained (1 520 and 1 492°C, respectively). These values were determined from the second derivate of the cooling curve obtained for the lowest cooling rate employed, Fig. 6, which was assumed to be close to the equilibrium condition; in this figure it is observed that the temperatures predicted can be associated to characteristic peaks appearing in the second derivative of the cooling curve. The latter curve exhibited a peak after which no thermal fluctuations were observed during the continuous cooling of the sample; this peak was associated with the end point of the peritectic transformation (1 472°C). In this way, it was possible to estimate the time

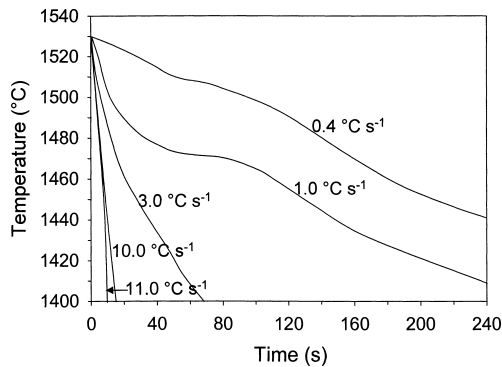


Fig. 4. Continuous cooling curves.

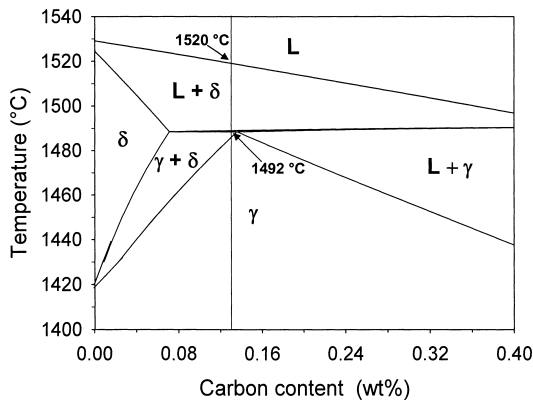


Fig. 5. Fe–C pseudo-binary diagram (1.15% Mn, 0.15% Si, 0.15% Cu).

elapsed in the solid–liquid region,  $t$ . The behavior showed by the cooling curve of Fig. 6 was systematically observed for all cooling rates. These results are presented in Table 2, which also includes the estimated  $\lambda$  values.

4.2. Simulation

The solidification simulation in terms of solid fraction evolution is shown in Fig. 7, which includes the predictive behavior for solidification under equilibrium conditions and Scheil’s microsegregation model. The start temperature of solidification (1 520°C) was the same in all cases because its evaluation was based on thermodynamic aspects considering the chemical composition of steel.

The start temperature of  $\gamma$  phase formation, indicated by the vertical dotted line, was not affected by the cooling rate and its value approached the equilibrium condition for all samples. This suggests that the initial formation of  $\gamma$  phase is not controlled by carbon diffusion into the liquid and that formation of  $\gamma$  phase occurs massively from the liquid at

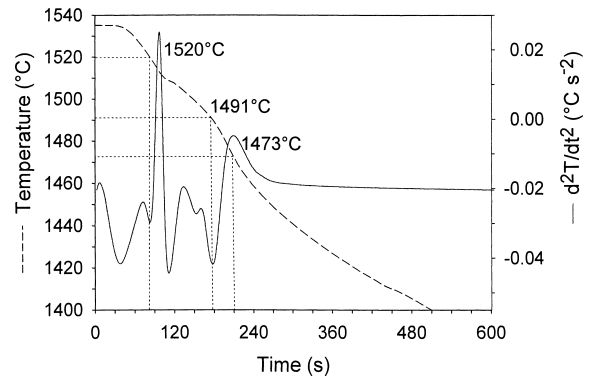


Fig. 6. The thermal analysis for the 0.4°C s<sup>-1</sup> cooling curve.

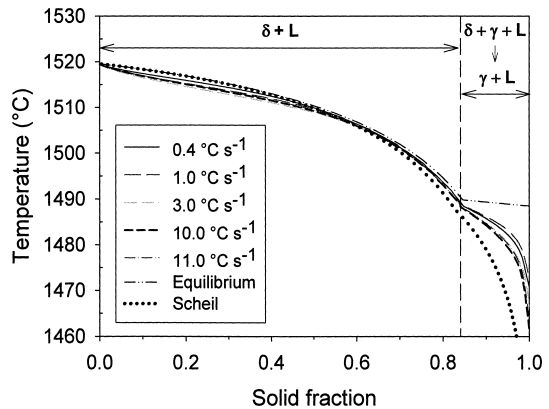
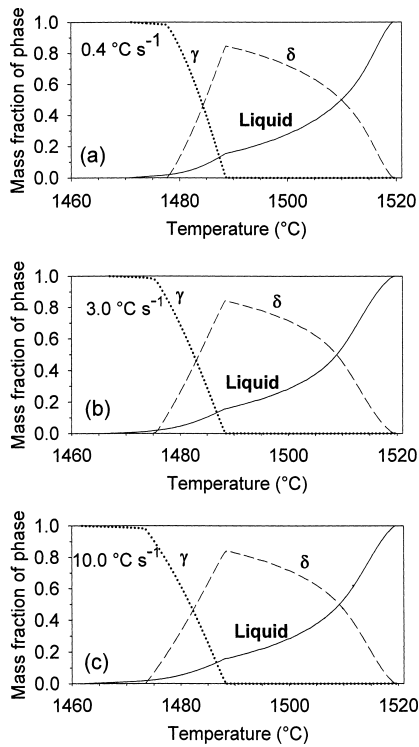


Fig. 7. Solid fraction evolution.

Table 2. Values obtained by thermal analyze of the curves continuous cooling.

Start temperature of solidification (°C)	End temperature of solidification (°C)	Solidification time, $t$ (s)	Secondary dendrite arm, $\lambda$ , ( $\mu\text{m}$ )	Cooling rate (°C s <sup>-1</sup> )
1520	1472	128	165	0.4
1522	1469	70	131	1.0
1523	1468	18	78	3.0
1520	1457	6.5	53	10.0
1521	1455	6	52	11.0



**Fig. 8.** Evolution of mass fraction of phase during solidification with the temperature for several cooling rates, (a)  $0.4^{\circ}\text{C s}^{-1}$ , (b)  $3.0^{\circ}\text{C s}^{-1}$  and (c)  $10.0^{\circ}\text{C s}^{-1}$ .

the interface between the  $\delta$  primary phase and the segregated liquid that surrounds it, in agreement with the mechanism known as “peritectic reaction”.<sup>6)</sup> On the other hand, the temperature for the end of solidification or peritectic transformation decreased with increasing cooling rate, and its value was found within a range limited by the equilibrium conditions and Scheil’s model, *i.e.* within the lowest and highest segregation levels. The temperature for the end of transformation were lower than those at equilibrium in 15 and 30°C, approximately, for extreme cooling rates of 0.4 and  $11^{\circ}\text{C s}^{-1}$ , respectively.

The temperature dependence of the mass fraction of phases is shown in **Fig. 8**, in which for the sake of clarity only the results obtained for cooling rates of 0.4, 3 and  $10^{\circ}\text{C s}^{-1}$  were included. It is seen that the fraction of  $\delta$  phase increases until the starting temperature for the peritectic reaction is reached, which is independent of the cooling rate. From this point onwards,  $\gamma$  phase grows at the expense of  $\delta$  phase and remaining liquid. In addition to that, it is seen that the temperatures at which  $\delta$  phase disappears and solidification ends are shifted toward lower values with increasing cooling rate. Comparing the results obtained for the cooling rates of 10 and  $11^{\circ}\text{C s}^{-1}$ ; it was observed that solidification ended at a temperature 2°C lower for the case of the fastest cooling rate. This anomalous behavior is thought to be associated with an early formation of a gap between the crucible wall and the solid metal skin in the case of the fastest cooling rate, which results in a decrease in the heat extraction, with a consequent solidification delay.

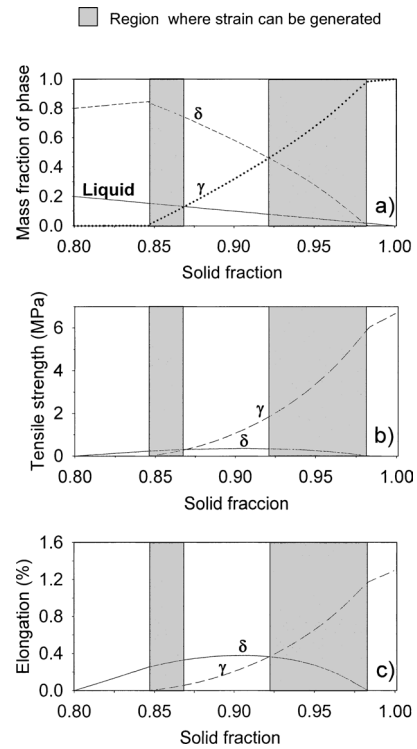


**Fig. 9.** Relationship between (a) mass fraction of phase, (b) tensile strength, (c) elongation, and solid fraction for peritectic carbon steel sample.

#### 4.3. Tensile Strength and Elongation during Solidification

In accordance with the peritectic transformation mechanism in which  $\delta$  and  $\gamma$  phases are in contact, it is supposed that the differences in the mechanical behavior of the phases at high temperatures can induce strains at their interfaces, with a consequent generation of cracks.<sup>9,10)</sup> Equations (2)–(5) were used with the aim of estimate the tensile strength and elongation for both phases as a function of solid fraction evolution. For illustration purposes, the results obtained for the sample with a cooling rate of  $11^{\circ}\text{C s}^{-1}$  are described, **Fig. 9**. The dark areas show the ranges of solid fraction with susceptibility to the generation of strains at the  $\delta/\gamma$  interface.

Figure 9(a) shows the mass fractions of  $\delta$  and  $\gamma$  phases for solid fractions at which strains were generated during solidification in the present study. For a solid fraction of 0.85, the fraction of  $\delta$  phase increased until  $\gamma$  phase begun forming. At higher solid fractions, the  $\delta$  phase fraction decreased, becoming equal to that of  $\gamma$  phase at a solid fraction of 0.92. Then,  $\delta$  phase disappeared at a solid fraction of 0.98, and an additional amount of  $\gamma$  phase was formed from the remaining liquid.

Figures 9(b) and 9(c) show the variation of tensile strength and elongation for  $\delta$  and  $\gamma$  phases with respect to solid fraction, respectively. In the solid fraction range of 0.85–0.87,  $\gamma$  phase showed the lowest values of tensile strength and elongation, which indicates that in this range the strain was generated in the  $\gamma$  phase. In the solid fraction range of 0.87–0.92,  $\delta$  phase showed a lower tensile strength and a higher elongation when compared to  $\gamma$  phase, consequently, in this solid fraction range the strain was not gener-

ated in any phase. At a solid fraction of 0.92, both phases  $\delta$  and  $\gamma$  had the same elongation. However, above the latter solid fraction  $\gamma$  phase exhibited higher tensile strength and higher elongation values than  $\delta$  phase. This suggests that in the solid fraction range of 0.92–0.98, the strain will be generated in the  $\delta$  phase.

The phase evolution, tensile strength and elongation of  $\delta$  and  $\gamma$  phases, with respect to the solid fraction, showed the same behavior for all cooling rates used. However, it is necessary to point out that the solid fraction changes occurred more rapidly when the cooling rate was increased, causing the formation of cracks at relatively low temperatures. In this way, in the continuous casting process of conventional slabs, the zones closer to the surface are the most susceptible to cracking because this zone has the severest cooling conditions.

The mechanic behavior illustrated in Fig. 9., *i.e.* the presence at two zones of crack susceptibility, agrees qualitatively with that observed by Mizukami<sup>9)</sup> in a carbon steel containing 0.14% C and a low alloy steel with 0.11% C, 0.5% Mn and 0.1% Si, for which the zones of crack susceptibility were found in solid fraction ranges of 0.88–0.92, 0.98–1, 0.94–0.965 for the former steel and 0.99–0.995 for the second one. For the case of the latter steel, Mizukami<sup>9)</sup> suggested that the end of solidification is marked by the formation of the  $\gamma$  phase from the liquid, as it was observed in the steel of the present work, which has a higher Mn content (1.15 wt%).

Estimations showed that under equilibrium conditions Mn causes a shift in the peritectic point toward lower C mass content values, decreasing at the same time the solid fraction/liquid fraction ratio at the temperature of peritectic transformation. In this way, in a hypo-peritectic steel where Mn segregation is high as in this work, the solidification mode can be modified to correspond to that for a hyper-peritectic steel, where  $\gamma$  phase is formed from liquid at the end of solidification. Thus, the peritectic transformation and consequently the crack susceptibility range are shifted toward lower solid fraction values.

#### 4.4. Contraction

The contraction level was calculated with the aid of Eq. (6), and its variation with solid fraction is shown in Fig. 10. This figure shows a progressive increase of contraction from a solid fraction of 0.85, for cooling rates higher than  $3^\circ\text{C s}^{-1}$ , showing a change in this behavior at values near a solid fraction of 0.98, where it shows an expansion instead of a contraction. The expansion levels were particularly important for cooling rates of 10 and  $11^\circ\text{C s}^{-1}$ . The highest contraction level was found at solid fraction values close to 0.98 in agreement with the end of peritectic transformation, which contributed to increase the crack susceptibility in the solid fraction range of 0.92–0.98 (Fig. 9).

The expansion observed at a solid fraction value of 0.98 is associated with the formation of  $\gamma$  phase from liquid as well as with the microsegregation level. The software was used to evaluate the mass content of the alloying elements in the solid at the solidification front as a function of solid fraction. For illustration purposes, Fig. 11 shows the results obtained for the case of Mn, which had the highest segregation index with respect to other elements. In this figure it is

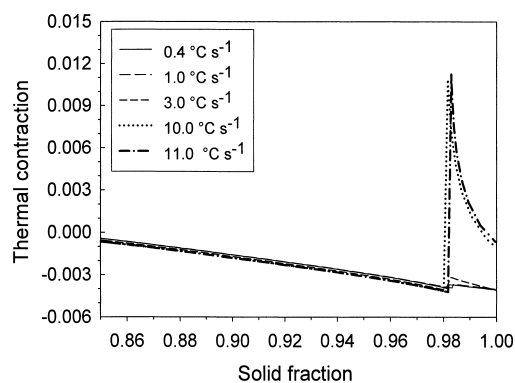


Fig. 10. Relationship between thermal contraction and solid fraction for several cooling rates.

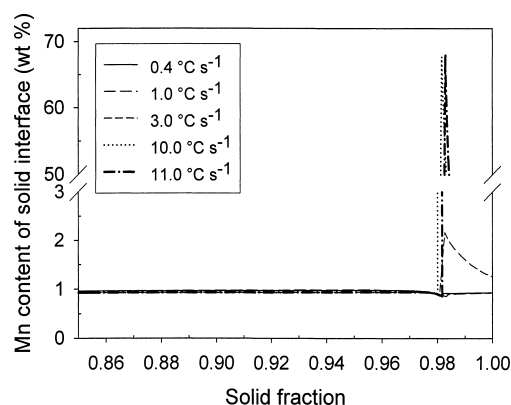


Fig. 11. Variation of Mn content at the interface solid–liquid with solid fraction for several cooling rates.

observed that at a cooling rate above  $3^\circ\text{C s}^{-1}$  microsegregation becomes important for solid fraction values close to 0.98.

## 5. Conclusions

From the description of the evolution of phases during solidification of a hypo-peritectic steel and from the mechanical behavior of this as a function of solid fraction, the following conclusions were drawn:

- (1) Crack susceptibility is dependent on the content of phases during solidification. Crack susceptibility occurred independently of cooling rate in two ranges of solid fraction (0.85–0.87 and 0.92–0.98), which were associated to the mechanical behavior of  $\gamma$  and  $\delta$  phases, respectively.
- (2) The highest contraction observed at the end of the peritectic transformation can be considered as an additional contribution to the crack susceptibility in the solid fraction range of 0.92–0.98.
- (3) An increase in cooling rate promotes crack susceptibility since it promotes a rapid evolution of the solid fraction.
- (4) At the end of solidification, the significant microsegregation of Mn observed for high cooling rates promoted both a change in the solidification mode, from a hypo-peritectic mode into a hyper-peritectic mode and the expansion of the solid formed from the remaining liquid.

REFERENCES

- 1) W. R. I. a. A. Perkins: Int. Conf. Organized by the Metals Society, London and L'Institut the Recherches de la Sidérurgie Francaise (IRSID), Biarritz, (1977), 330.
- 2) J. K. Brimacombe, F. Weinberg and E. B. Hawbolt: Continuous Casting Heat Flow, Solidification and Crack Formation, 2, I. S. S. o. AIME, ed. by BookCrafters, Chelsea, U.S.A., (1984), 215.
- 3) S. K. Mishra Pathak, S. Das and S. Ranganthan: *Mater. Sci. Eng. A*, **A323** (2002), 285.
- 4) J. Konishi, M. Militzer, J. K. Brimacombe and I. V. Samarasekera: *Metall. Mater. Trans. B*, **33B** (2002), 413.
- 5) C. Cicutti and R. Boerl: *Steel Res. Int.*, **77** (2006), 194.
- 6) D. M. Stefanescu: *ISIJ Int.*, **46** (2006), 786.
- 7) Y. M. Won and B. G. Thomas: *Metall. Mater. Trans. A*, **32A** (2001), 1755.
- 8) Y. M. Won, H. N. Han, T. J. Yeo and K. H. Oh: *ISIJ Int.*, **40** (2000), 129.
- 9) H. Mizukami, A. Yamanaka and T. Watanabe: *ISIJ Int.*, **42** (2002), 964.
- 10) H. Mizukami, Y. Shirai and A. Yamanaka: *ISIJ Int.*, **46** (2006), 1040.
- 11) D. Brody and C. Flemings: *Trans. Metall. Soc. AIME*, **236** (1966), 615.
- 12) W. Clyne and W. Kurz: *Metall. Trans. A*, **12A** (1981), 965.
- 13) Y. Ueshima, S. Mizoguchi, T. Matsumiya and H. Kajioka: *Metall. Trans. B*, **17B** (1986), 845.
- 14) J. Miettinen: *Scand. J. Metall.*, **22** (1993), 317.
- 15) J. Miettinen: *Metall. Mater. Trans. B*, **28B** (1997), 281.
- 16) DICTRA software, Tool for Simulation of Diffusional Transformations in Alloys, 24, Foundation of Computational Thermodynamics, Stockholm-Sweden, (2006).
- 17) A. Thermo-Calc software, The Phase Diagram in Alloys Multicomponents, R, Foundation of Computational Thermodynamics, Stockholm-Sweden, (2006).
- 18) A. Jablonka, K. Harste and K. Schwerdtfeger: *Steel Res.*, **62** (1991), 24.
- 19) S. Louhenkilpi, J. Miettinen and L. Holappa: *ISIJ Int.*, **46** (2006), 914.